Harmonic Amplification Analysis of Cable Lines with Distributed Parameters Based on Kalman Filter and Convolution Inversion

Yang Pu, Qin Shu, *Member*, *IEEE*, and Fangwei Xu, *Member*, *IEEE*

***Abstract*—Harmonic amplification phenomena could appear at the point of common connection (PCC) of the cable line terminal. However, the distributed parameter model of the cable line contains hyperbolic functions with plural variables, which makes it challenging to obtain the harmonic amplification factor (HAF). Hence, a time-domain method combining the Kalman filter and convolution inversion (KFCI) methods is proposed to address this problem. First, the Kalman filter method optimizes the square wave pulse response (SWPR) with measurement error. Then, the optimized SWPR data are used to get the HAF by the convolution inversion method. Next, the harmonic amplification characteristics of cable lines are explored. Finally, an experimental simulation model is built on the PSCAD software, verifying the optimization effectiveness of Kalman filter for the SWPR with error and the accuracy of the HAF calculated by the proposed method. The analysis rationality of harmonic amplification properties is also demonstrated.**

***Index Terms*—Cable line, distributed parameters, Kalman filter, convolution inversion, harmonic amplification.**

I. Introduction

IN modern electric energy systems such as wind farms and solar parks, the power generation and power grid could generate harmonics with wide-band frequency [1]-[4]. The wide-band resonance phenomenon would be induced due to numerous cable lines in the power system interacting with the impedance of the power grid or clean energy generation [5]-[7]. Likewise, the broadband frequency harmonics generated can be excited, leading to harmonic amplification phenomenon, which results in power quality problems [8]-[10]. Hence, the power quality problem caused by harmonic amplification becomes prominent with the rising proportion of clean energy and cable lines.

For cable lines in the high-voltage alternating current (HVAC) transmission power system, the resonance can be induced by the impedance interaction among the sending generation, cable line, and power grid [11]. In [12], the harmonic resonance problem of wind parks is explored using the sensitivity analysis method, and a resonance-suppressing plan is proposed based on the frequency offset method. In [13], it is suggested that the singularity of a network admittance matrix of modal sensitivity is related to system resonance. And the minimum eigenvalue of the matrix is used to identify harmonic resonance. In [14], based on the passivity-based analysis method, the grid-tied inverters are designed considering the capacitance of the cable line to get robustness characteristics. In [15], it is disclosed that harmonics generated from the grid-connected photovoltaic plant can be amplified with cable lines. Meanwhile, the harmonics have the feature of wide-band frequency. In [16], the cable line is modeled as multiple π units for high-frequency resonance analysis based on impedance method. Generally, when the distributed parameters of cable lines are not considered, the modal analysis and impedance methods are applicable. Otherwise, only the impedance method is applicable when the distributed parameters of cable lines are considered. However, it is arduous for calculation [17], [18].

In [19], for scenarios where cable lines with distributed parameters are considered, the stability problem in the voltage source converter based high-voltage direct current (VSC-HVDC) transmission system is studied using the Nyquist criterion. The conclusion presents that distributed parameter models of cable lines in the high-frequency scene is more accurate. In [20], it is indicated that the capacitance of the cable line and the inductance of the power grid can induce system resonance. And the damping method is proposed for the resonance peaks. In [21], a practical circuit considering all phases of the asymmetry power line is established for the compensated distributed networks using impedance modeling method. In [22], the frequency-length factor is proposed to investigate the harmonic amplification considering the distributed parameters of ultra-long distance transmission lines. Generally, few deliberations have been paid into the scenario of the harmonic amplification of the cable line from one side terminal to another side terminal when the power at dual ends performs simultaneously.

Inspired by the aforementioned methods and unconsidered scenarios, we propose a time-domain method to explore har-

Manuscript received: July 24, 2022; revised: September 28, 2022; accepted: January 30, 2023. Date of CrossCheck: January 30, 2023. Date of online publication: April 21, 2023.

This work was supported in part by Natural Science Foundation of China (No. 52277113).

This article is distributed under the terms of the Creative Commons Attribution 4.0 International License (http://creativecommons.org/licenses/by/4.0/).

Y. Pu, Q. Shu, and F. Xu (corresponding author) are with the College of Electrical Engineering, Sichuan University, Chengdu 610065, China (e-mail: 363392158@qq.com; shuqin@scu.edu.cn; xufangwei@scu.edu.cn)

DOI: 10.35833/MPCE.2022.000445

monic amplification characteristics considering the distributed parameters of cable lines. The main contributions of this research are as follows.

1) The convolution inversion method [23] integrated with the Kalman filter (KF) method can be applied to obtain the harmonic amplification factor (HAF) using the square wave pulse response (SWPR) data with error.

2) The harmonic amplification characteristics considering the distributed parameters of cable lines in a typical HVAC grid-connected (HVACG) system are explored.

3) The harmonic amplification characteristics obtained can be a reference for damper designing in practical engineering.

The rest of this paper is organized as follows. In Section II, a typical HVACG system model and the corresponding dynamic equations are established. In Section III, the basic theory based on KF and convolution inversion (KFCI) methods is presented. Then, the harmonic amplification characteristics are studied in Section IV. Next, simulation experiments are described in Section V. Finally, the conclusions of this paper are presented in Section VI.

II. HVACG System Model and Corresponding Dynamic Equations

Figure 1 shows a typical HVACG system consisting mainly of power generator, transformer, HVAC feeder, load, and power grid. The load consists of an active load P and a reactive load Q. The power grid covers a power supply in series with an impedance. A bus bar brings the load and grid together at the point of common connection (PCC).

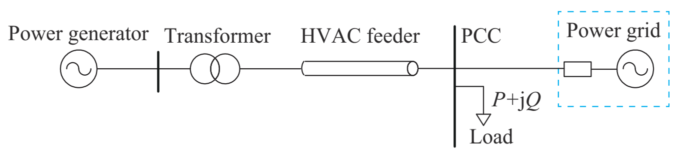

Fig. 1. A typical HVACG system.

Figure 2 shows the equivalent circuit of the HVACG system. u_s and Z_0 represent the power source and impedance that the power generator motor and transformer are equivalent to by the Thevenin's theorem [24], respectively. Z_0 consists of the resistance r_w, inductance l_w, and capacitance c_w. u_w represents the voltage of capacitance c_w. The power grid is equivalent to a current source i_g in parallel with an impedance Z_g that consists of resistance r_g and inductance l_g [25], [26]. For the distributed parameter model of the cable line, r_0, l_0, and c_0 represent the per-unit-length resistance, per-unit-length inductance, and per-unit-length capacitance, respectively [27], [28]. $u_{0(1)}$, $u_{0(2)}$, …, $u_{0(n-1)}$ and $i_{0(1)}$, $i_{0(2)}$, …, $i_{0(n)}$ represent the node voltages and currents flowing in the unite π segment of the cable line, respectively. n represents the amount of equivalent π units of the cable line. i_1 and i_2 represent the currents flowing through the cable line. u_1 and u_2 represent the terminal voltages of the cable line.

As observed from Fig. 2, the dynamic equations of the typical HVACG system with a l km length cable line can be expressed as [23]:

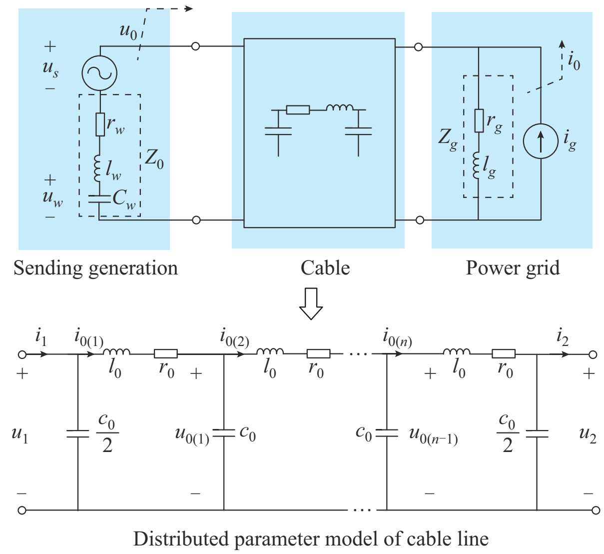

Fig. 2. Equivalent circuit of HVACG system.

$$\begin{cases} u_1 = u_s + u_w - i_1 r_w - l_w \dfrac{\mathrm{d}i_1}{\mathrm{d}t} \\ i_1 = -c_w \dfrac{\mathrm{d}u_w}{\mathrm{d}t} \\ i_1 - i_{0(1)} = \dfrac{c_0}{2}\dfrac{\mathrm{d}u_1}{\mathrm{d}t} \\ u_1 - u_{0(1)} = l_0 \dfrac{\mathrm{d}i_{0(1)}}{\mathrm{d}t} + r_0 i_{0(1)} \\ i_{0(1)} - i_{0(2)} = c_0 \dfrac{\mathrm{d}u_{0(1)}}{\mathrm{d}t} \\ \vdots \\ u_{0(n-1)} - u_2 = l_0 \dfrac{\mathrm{d}i_{0(n)}}{\mathrm{d}t} + r_0 i_{0(n)} \\ i_2 = i_{0(n)} - \dfrac{c_0}{2}\dfrac{\mathrm{d}u_2}{\mathrm{d}t} \\ u_2 = l_g\left(\dfrac{\mathrm{d}i_2}{\mathrm{d}t} + \dfrac{\mathrm{d}i_g}{\mathrm{d}t}\right) + r_g(i_2 + i_g) \end{cases} \tag{1}$$

III. Basic Theory Based on KFCI

A. Optimization for State Variables Based on KF Method

The KF method is used to optimize the SWPR with error in this subsection.

The state space equation of the HVACG system can be expressed as:

$$\begin{cases} \dot{\boldsymbol{x}} = \boldsymbol{A}\boldsymbol{x} + \boldsymbol{B}\boldsymbol{u} \\ \boldsymbol{y} = \boldsymbol{C}\boldsymbol{x} \end{cases} \tag{2}$$

where $\boldsymbol{x}$, $\boldsymbol{u}$, and $\boldsymbol{y}$ represent the state vector, input vector, and output vector, respectively; and $\boldsymbol{A}$, $\boldsymbol{B}$, and $\boldsymbol{C}$ represent the coefficient matrices.

According to (1), $n=2$ is set and the matrices $\boldsymbol{A}$, $\boldsymbol{B}$, and $\boldsymbol{C}$ can be obtained as:

$$\boldsymbol{A}=\begin{bmatrix} 0 & -\frac{4}{lc_0} & 0 & 0 & 0 & 0 & \frac{4}{lc_0} & 0 \\ \frac{2}{ll_0} & -\frac{r_0}{l_0} & 0 & -\frac{2}{ll_0} & 0 & 0 & 0 & 0 \\ 0 & 0 & -\frac{r_0}{l_0} & \frac{2}{ll_0} & -\frac{2}{ll_0} & 0 & 0 & 0 \\ 0 & \frac{2}{lc_0} & -\frac{2}{lc_0} & 0 & 0 & 0 & 0 & 0 \\ 0 & 0 & \frac{4}{lc_0} & 0 & 0 & 0 & 0 & -\frac{4}{lc_0} \\ 0 & 0 & 0 & 0 & 0 & 0 & -\frac{1}{c_w} & 0 \\ -\frac{1}{l_w} & 0 & 0 & 0 & 0 & \frac{1}{l_w} & -\frac{r_w}{l_w} & 0 \\ 0 & 0 & 0 & 0 & \frac{1}{l_g} & 0 & 0 & -\frac{r_g}{l_g} \end{bmatrix} \tag{3}$$

$$\boldsymbol{B}^{\mathrm{T}}=\begin{bmatrix} 0 & 0 & 0 & 0 & 0 & 0 & \frac{1}{l_w} & 0 \\ 0 & 0 & 0 & 0 & \frac{2}{c_0} & 0 & 0 & 0 \end{bmatrix} \tag{4}$$

$$\boldsymbol{C}=\begin{bmatrix} 1 & 0 & 0 & 0 & 0 & 0 & 0 & 0 \\ 0 & 0 & 0 & 0 & 1 & 0 & 0 & 0 \\ 0 & 0 & 0 & 0 & 0 & 0 & 1 & 0 \\ 0 & 0 & 0 & 0 & 0 & 0 & 0 & 1 \end{bmatrix} \tag{5}$$

The state variable vector can be expressed as:

$$\boldsymbol{x}^{\mathrm{T}}=\begin{bmatrix} u_{1n} & i_{0(1)} & i_{0(2)} & u_{0(1)} & u_{2n} & u_w & i_{1n} & i_{2n} \end{bmatrix} \tag{6}$$

where u_{1n}, u_{2n} and i_{1n}, i_{2n} represent the measured voltages and currents of the terminal of the cable line, respectively.

The excitation vector $\boldsymbol{u}$ should be determined according to the actual injection situation: $\boldsymbol{u}=[u_0, 0]$ when square wave pulse excitation (SWPE) u_0 is injected; $\boldsymbol{u}=[0, i_0]$ when SWPE i_0 is injected; and $\boldsymbol{u}=[u_0, i_0]$ when SWPEs u_0 and i_0 are injected synchronously.

The reason $l_g \mathrm{d}i_g/\mathrm{d}i_t$ is omitted from (1) to (3) is that the SWPE i_0 is a constant current source except for the period of the rising and falling edges. However, the period of rising and falling edges lasts briefly (only 2.5 ns in the experimental process), which would not affect the results seriously.

According to the state space equation (2), the state estimation equation and observation equation can be expressed as (7) and (8), respectively.

$$\boldsymbol{x}_k=\boldsymbol{A}'\boldsymbol{x}_{k-1}+\boldsymbol{B}'\boldsymbol{u}_k+\boldsymbol{Q}_k \tag{7}$$

$$\boldsymbol{y}_k=\boldsymbol{C}'\boldsymbol{x}_k+\boldsymbol{R}_k \tag{8}$$

where $\boldsymbol{y}_k=[u_{1n}, u_{2n}, i_{1n}, i_{2n}]$ represents the vector of measurements; $\boldsymbol{x}_k$ and $\boldsymbol{u}_k$ represent the discrete state vector and input vector, respectively; $\boldsymbol{R}_k$ represents the observation error caused by the harmonics, instrumentation precision, or Gaussian noise, of which the covariance matrix is represented as $\boldsymbol{R}$; and $\boldsymbol{Q}_k$ represents the model error that is caused by cable aging or the accuracy of the model establishment, of which the covariance matrix is represented as $\boldsymbol{Q}$. For instance, the infinite π distributed parameter model is approximated as a model with two π sections in (3).

Equations (7) and (8) can be used to estimate the state variable vector $\boldsymbol{x}$ by the KF method as follows.

1) The prediction vector of prior state variables $\boldsymbol{x}_k^-$ and its covariance matrix $\boldsymbol{P}_k^-$ can be expressed as:

$$\boldsymbol{x}_k^-=\boldsymbol{A}'\boldsymbol{x}_{k-1}^+ +\boldsymbol{B}'\boldsymbol{u}_k^+ \tag{9}$$

$$\boldsymbol{P}_k^-=\boldsymbol{A}\boldsymbol{P}_{k-1}^+\boldsymbol{A}^{\mathrm{T}}+\boldsymbol{Q} \tag{10}$$

where the superscripts + and − represent the posteriori and priori estimation symbols, respectively; and the covariance matrix of the model noise is set as $\boldsymbol{Q}=\boldsymbol{B}'\boldsymbol{R}\boldsymbol{B}^{\mathrm{T}}$.

2) The KF gain can be expressed as:

$$\boldsymbol{M}=\boldsymbol{P}_k^-\boldsymbol{C}^{\mathrm{T}}(\boldsymbol{C}'\boldsymbol{P}_k^-\boldsymbol{C}^{\mathrm{T}}+\boldsymbol{R})^{-1} \tag{11}$$

3) The vector of posterior state variables $\boldsymbol{x}_k^+$ and its covariance matrix $\boldsymbol{P}_k^+$ can be updated as:

$$\boldsymbol{x}_k^+=\boldsymbol{x}_k^- +\boldsymbol{M}(\boldsymbol{y}_k-\boldsymbol{C}'\boldsymbol{x}_k^-) \tag{12}$$

$$\boldsymbol{P}_k^+=(\boldsymbol{I}-\boldsymbol{M}\boldsymbol{C}')\boldsymbol{P}_k^- \tag{13}$$

where $\boldsymbol{I}$ represents the identity matrix.

According to (12), the vector of optimization results can be obtained as:

$$\boldsymbol{v}=\boldsymbol{C}'\boldsymbol{x}_k^+ \tag{14}$$

where $\boldsymbol{v}=[u_{1op}, u_{2op}, i_{1op}, i_{2op}]$ represents the optimized vector of $\boldsymbol{y}_k$.

B. Convolution Inversion Method for Amplitude-frequency Characteristics

According to [23], the convolution inversion method can be used to calculate the amplitude-frequency characteristics, and the convolution relationship can be expressed as:

$$\boldsymbol{v}(n)=\rho(n)\otimes\boldsymbol{h}(n) \quad n\in\mathbb{Z} \tag{15}$$

where ρ represents the SWPE; and $\boldsymbol{h}=[h_1, h_2, h_3, h_4]$. h_1, h_2, h_3, and h_4 are the unit impulse responses (UIRs) from the SWPE to u_{1op}, u_{2op}, i_{1op}, and i_{2op}, respectively. Then the optimal UIR can be obtained as (16) by the convolution inversion method.

$$\hat{\boldsymbol{h}}=(\boldsymbol{J}^{\mathrm{T}}\boldsymbol{J})^{-1}\boldsymbol{J}^{\mathrm{T}}\boldsymbol{v} \tag{16}$$

where $\boldsymbol{J}$ represents the excitation matrix, which can be found in the Appendix A.

The amplitude-frequency characteristics $\boldsymbol{G}(k)=[G_{u_1}(k), G_{u_2}(k), G_{i_1}(k), G_{i_2}(k)]$ can be obtained by the discrete Fourier transform (DFT) using data $\hat{\boldsymbol{h}}$. $G_{u_1}(k)$, $G_{u_2}(k)$, $G_{i_1}(k)$, and $G_{i_2}(k)$ represent the amplitude-frequency characteristics from SWPE to u_{1op}, u_{2op}, i_{1op}, and i_{2op}, respectively.

The pseudocode of the KFCI for amplitude-frequency characteristics is given as Algorithm 1.

IV. Harmonic Amplification Characteristic Analysis of Cable Lines

Section III presents a method to estimate the amplitude-frequency characteristics. For exploring the harmonic amplification phenomena, the basic theory would be used to obtain the HAF in the actual scenarios.

Algorithm 1: pseudocode of the KFCI
Extract the SWPR data $\boldsymbol{y}_k$
Set cable line as n units (n=2)
Create the state space matrices $\boldsymbol{A}$, $\boldsymbol{B}$, and $\boldsymbol{C}$
Discretize the state space matrices $\boldsymbol{A}'$, $\boldsymbol{B}'$, and $\boldsymbol{C}'$
Calculate the prediction vector of prior state variables $\boldsymbol{x}_k^-$
Update the prior covariance matrix $\boldsymbol{P}_k^-$
Update the KF gain $\boldsymbol{M}$
Update the posterior covariance matrix $\boldsymbol{P}_k^+$
Update the vector of posterior state variables $\boldsymbol{x}_k^+$
Output $\boldsymbol{v}$
Deconvolve with $\boldsymbol{v}$ and SWPE data
Obtain UIR $\hat{\boldsymbol{h}}$
Obtain the amplitude-frequency characteristics $\boldsymbol{G}(k)$ by DFT

A. Extraction of SWPR Data

The data extraction steps are provided as follows.

Step 1: before injecting the SWPE, the voltage (u_1, u_2) and current (i_1, i_2) data of the cable line terminals for a period of time are extracted first, as shown in Fig. 2.

Step 2: the SWPE (u_0, i_0) is injected into the HVACG system after an integer multiple of the fundamental wave period. Meanwhile, we extract the data (u_1, u_2, i_1, i_2) with the same duration as *Step 1* again, beginning with the injection time point of SWPE.

The injected u_0 and i_0 are SWPEs with the same amplitude and pulse width (PW). Meanwhile, u_0 is injected in series with u_s, and i_0 is injected in parallel with i_g. And the specific injection u_0 or i_0 would be introduced later according to the actual scenarios.

Step 3: the SWPR can be obtained by subtracting the two sets of data obtained in *Steps 1* and *2*, which can be represented as u_{1n}, u_{2n}, i_{1n}, and i_{2n}, respectively. After the subtraction process, the power sources u_g and i_g are replaced as u_0 and i_0, respectively.

The SWPE data can be generated with the information of sampling frequency and PW directly by the software, which do not need to be extracted from the model.

B. Derivation Process of HAF

The relationship of excitation-response in the frequency domain can be expressed as:

$$X_1(k) = U(k)G_{x_1}(k) \tag{17}$$

$$X_2(k) = U(k)G_{x_2}(k) \tag{18}$$

where $U(k)$ represents the excitation (u_0 or i_0); $X_1(k)$ and $X_2(k)$ represent the responses (u_1 and u_2 or i_1 and i_2); and $G_{x_1}(k)$ and $G_{x_2}(k)$ represent the amplitude-frequency characteristics accordingly.

According to (17) and (18), the HAF from $X_1(k)$ to $X_2(k)$ can be expressed as:

$$H_{x_2x_1} = \left|\frac{G_{x_2}(k)}{G_{x_1}(k)}\right| \tag{19}$$

According to extraction processes of SWPR data, the injection of SWPE can be divided into two ways for HAF, considering the operation of different power sources.

1) Single power supply considered: only u_0 or i_0 needs to be injected for excitation when calculating the HAF.

2) Dual power supply considered: in the regular operation of an actual HVACG system, HAF can be obtained using the SWPR data of u_0 and i_0 injected synchronously.

To illustrate the equivalent circuit change due to SWPE injection and SWPR extraction processes, the HVACG system is re-depicted, as shown in Fig. 3. The circuits depicted in Fig. 3(a), (b) and (c) describe the processes of *Steps 1*, *2*, and *3*, respectively. Z and Y represent the impedance and admittance of the cable line, respectively. i_0 and u_0 are injected in parallel with the current source i_g and in series with the voltage source u_s, respectively. The parameters (PW, sampling frequency) of the injected SWPE are the same. The relationship of the SWPE and SWPR can be depicted as the circuit shown in Fig. 3(c).

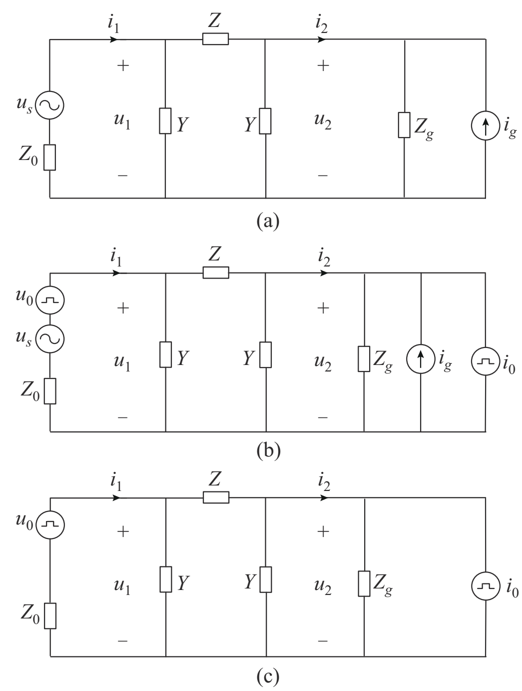

Fig. 3. Equivalent circuits before or after SWPE injection and SWPR extraction processes. (a) Before SWPE injection. (b) After SWPE injection. (c) After SWPR extraction.

By the superposition theorem, the relationship between the SWPE and SWPR can be obtained as:

$$\begin{cases} X_{11} = G_1 I_0 \\ X_{12} = G_2 U_0 \\ X_{21} = G_3 I_0 \\ X_{22} = G_4 U_0 \end{cases} \tag{20}$$

where $X_{11}+X_{12}=X_1$ and $X_{21}+X_{22}=X_2$; I_0 and U_0 represent the frequency domain expressions of i_0 and u_0, respectively; and G_1, G_2, G_3, and G_4 represent the supposed intermediate transfer function (TF) variables.

Generally, to obtain the HAF in different scenarios, the way of injecting SWPE and extracting SWPR is listed in Table I. It needs to mention that the capital letters G and H represent the HAFs of single power supply and dual power supply, respectively.

TABLE I
HAF IN DIFFERENT SCENARIOS

HAF	X_1	X_2	U
H_{uu}	u_1	u_2	u_0, i_0
H_{ii}	i_1	i_2	u_0, i_0
G_{u_1}	u_1		u_0
G_{u_2}		u_2	u_0
G_{i_1}	i_1		i_0
G_{i_2}		i_2	i_0

With the regulation for obtaining HAF and parameters listed in Table II, the analysis of HAF for voltage and current is represented as follows.

TABLE II
PARAMETERS OF PROTOTYPE

Parameter	Value
Voltage of AC voltage source	220 kV
Sending resistance	100 Ω
Sending inductance	0.1 H
Sending capacitance	10^{-6} F
Cable resistance per cell	0.031 Ω
Cable inductance per cell	0.406 mH
Cable capacitance per cell	0.179 μF
Current of AC current source	0.5 kA
Receiving resistance	190 Ω
Receiving inductance	10^{-6} H
PW of SWPE	0.8 ms

C. HHAF of Voltage

The HAF of the voltage at terminals of the cable line is represented as H_{uu}, which can be obtained as (21) according to (19) and (20).

$$H_{uu}=\left|\frac{U_2}{U_1}\right|=\left|\frac{(G_3+G_4)I_0}{(G_1+G_2)I_0}\right|=\left|\frac{(G_3+G_4)U_0}{(G_1+G_2)U_0}\right| \tag{21}$$

where U_1 and U_2 represent the frequency domain expressions of u_1 and u_2, respectively; and G_3+G_4 and G_1+G_2 represent the frequency characteristics from SWPE (u_0 and i_0 perform simultaneously) to u_2 and u_1, respectively. To obtain G_3+G_4 or G_1+G_2, the SWPR should be the response with u_0 and i_0 acting simultaneously. Meanwhile, the SWPE data can be either u_0 or i_0, according to (21).

Figure 4 illustrates the HAF curves of voltage with the cable line lengths of 24 km, 36 km, and 50 km. It can be observed from Fig. 4(a) that: when $l=24$ km, the curve has two resonance points impending the 10th and 50th harmonic orders; when $l=36$ km, it has two resonance points impending the 10th and 33rd harmonic orders; and when $l=50$ km, it has three resonance points impending the 10th, 24th, and 46th harmonic orders. The three curves all have resonance points around the 10th harmonic order. Meanwhile, G_{u_1} exceeding the resonance point around the 10th harmonic decreases gradually with the increase of the cable length. G_{u_1} at the resonance point with the high harmonic order is smaller than that with the low harmonic order. G_{u_1} is less than 1, and can be reduced to about 0. As observed in Fig. 4(b), G_{u_2} has the same property with G_{u_1}. In Fig. 4(c), H_{uu} at the first resonance points exceeds 1. And the longer the cable length is, the smaller the frequency interval between two adjacent resonance points is.

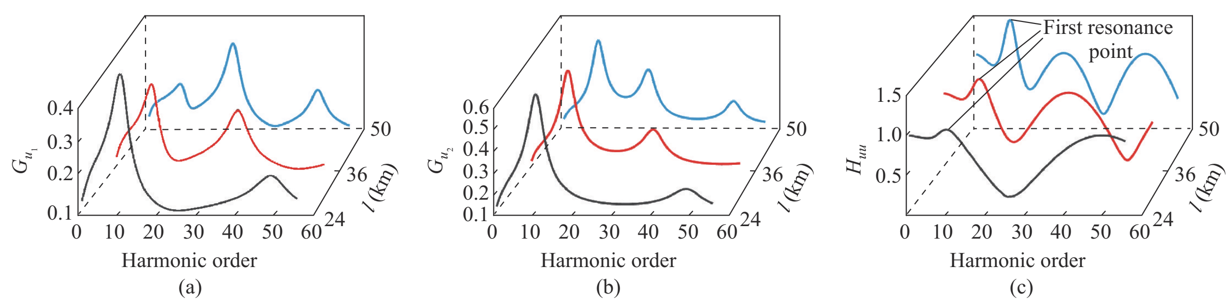

Fig. 4. HAF curves of voltage with different cable line lengths. (a) G_{u_1}. (b) G_{u_2}. (c) H_{uu}.

In Fig. 5, for the case of $l=24$ km, the HAF from u_1 to u_2 is shown with different values of r_0, l_0, and c_0. For exploring the influence of distributed parameters on harmonic amplification, one parameter is altered with other parameters fixed as 1 p.u.. For instance, when changing r_0, l_0 and c_0 are both set to be 1 p.u., and the corresponding result is shown in Fig. 5(a). The resonance trough in Fig. 5(a) fixes at the same frequency with different r_0. And the H_{uu} decreases slightly with the increase of r_0 at the resonance point. In Fig. 5(b), when l_0 decreases, the resonance trough moves towards the high harmonic order. Meanwhile, the value of the resonance trough decreases with the increase of l_0. As observed from Fig. 5(c), The change of c_0 has similar harmonic amplification characteristics to that of l_0.

D. HAF of Current

Similar to the derivation process for HAF of voltage, the HAF of current from i_1 to i_2 (H_{ii}) can be expressed as:

$$H_{ii}=\left|\frac{I_2}{I_1}\right|=\left|\frac{G_{i_2}I_0}{G_{i_1}I_0}\right|=\left|\frac{G_{i_2}U_0}{G_{i_1}U_0}\right| \tag{22}$$

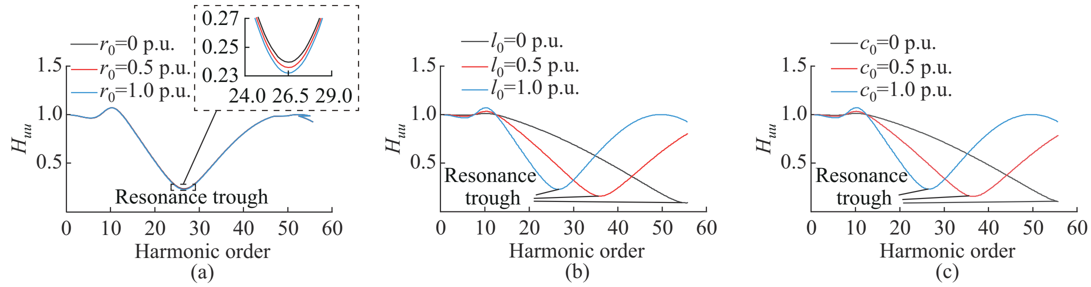

Fig. 5. H_{uu} with different distributed parameters. (a) $l_0 = 1$ p.u. and $c_0 = 1$ p.u.. (b) $r_0 = 1$ p.u. and $c_0 = 1$ p.u.. (c) $r_0 = 1$ p.u. and $l_0 = 1$ p.u..

where I_1 and I_2 represent the frequency domain expression of i_1 and i_2, respectively; and G_{i_1} and G_{i_2} represent the frequency characteristics from SWPE (u_0 and i_0 perform simultaneously) to i_1 and i_2, respectively.

Figure 6 illustrates the HAF curves of current along with the cable lengths of 24 km, 36 km, and 50 km. In Fig. 6(a), the first resonance trough appears around the 10th harmonic order. Meanwhile, G_{i_1} increases with the cable line at the 10th harmonic order. As the harmonic order increases, G_{i_1} approaches 1. In Fig. 6(b), G_{i_2} decreases to about 0.2 and then the phenomenon of interval fluctuation occurs. Meanwhile, they oscillate more seriously along the increasing cable line, and the first resonance trough appears at the 10th harmonic order. In Fig. 6(c), the first resonance trough decreases to 0.57 at the 9th harmonic order, and the second resonance trough moves toward lower harmonic order along with increasing cable length. The HAF exceeds 1 except at the harmonic order near the resonance trough.

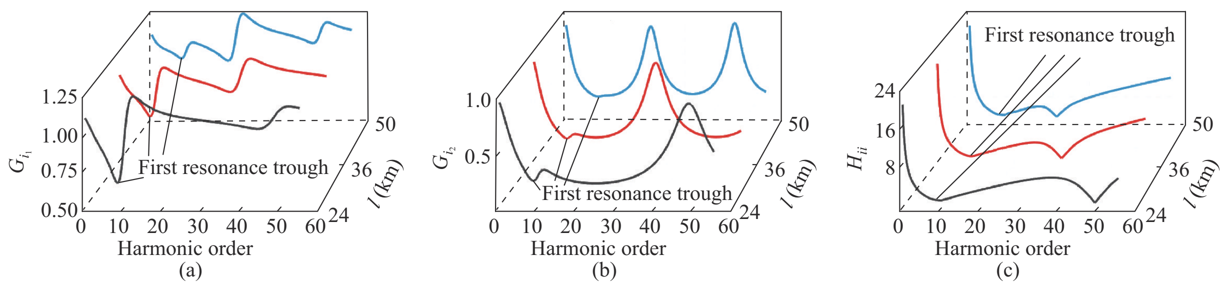

Fig. 6. HAF curves of current with different cable lengths. (a) G_{i_1}. (b) G_{i_2}. (c) H_{ii}.

Figure 7 illustrates the HAF curves of current with different distributed parameters (r_0, l_0, and c_0) of the cable line for the case of $l = 24$ km. In Fig. 7(a), H_{ii} curves coincide completely at different harmonic orders. The resonance troughs of H_{ii} decrease slightly with the increase of r_0. Meanwhile, the resonance trough is present at the same frequency. In Fig. 7(b), the H_{ii} curves coincide well at about the 0th-35th harmonic orders. The second resonance trough appears only with l_0 of 1 p.u., which means that the increase of l_0 can induce the HAF oscillation more intensely. c_0 and l_0 have the same effect on the HAF, as observed in Fig. 7(b) and (c).

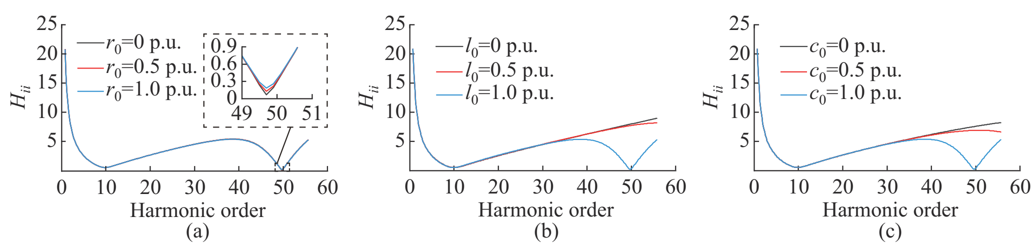

Fig. 7. H_{ii} with different distributed parameters. (a) $l_0 = 1$ p.u. and $c_0 = 1$ p.u.. (b) $r_0 = 1$ p.u. and $c_0 = 1$ p.u.. (c) $r_0 = 1$ p.u. and $l_0 = 1$ p.u..

Compared with H_{uu}, H_{ii} decreases intensely from the fundamental frequency to the first resonant trough. Conversely, H_{uu} slightly increases from the fundamental frequency to the first resonance point.

E. Results and Discussion

In this subsection, we present a comparative test for exploring the effect of the injection of SWPE on HAF. And the HAF at cable line terminals is set as the discussing object. The test is implemented based on three injection schmes: ① scheme 1, only current SWPE is injected; ② scheme 2, only voltage SWPE is injected; and ③ scheme 3, both current SWPE and voltage SWPE are injected.

In Fig. 8, HAF curves obtained by the three schemes are present. In Fig. 8(a), it can be observed that schemes 1 and 2 coincide well when exceeding the 30th harmonic order, and the HAF curves have a slight discrepancy at less than the 30th harmonic order. The scheme 3 significantly differs from schemes 1 and 2. In Fig. 8(b), it can be observed that the curves have huge differences except at the 11st and 49th harmonic orders. Hence, both current SWPE and voltage SWPE should be injected for obtaining the HAF at cable line terminals in the case that the voltage and current supplies act simultaneously.

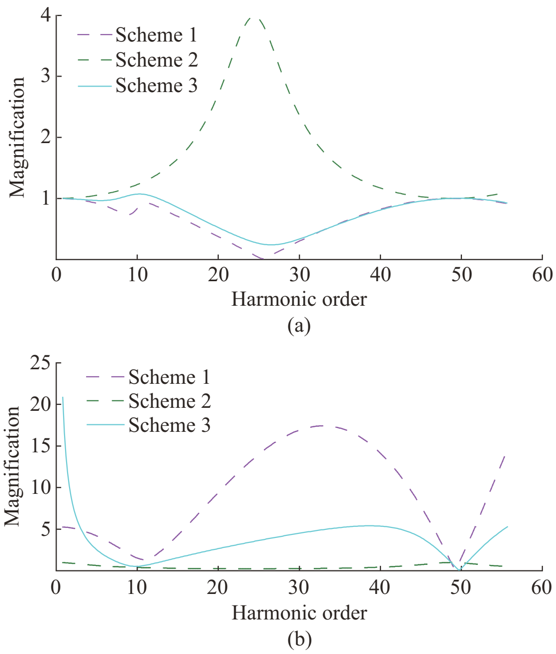

Fig. 8. HAF curves at cable line terminals obtained by different schemes. (a) H_{uu}. (b) H_{ii}.

V. Experiment Verification

A simulation model for HVACG system is carried out on PSCAD software, which is used to validate the effectiveness and rationality of the KFCI method on analyzing the harmonic amplification characteristics. The configuration and parameters of the model are shown in Fig. 2 and Table II, respectively. The cable line is equivalent to n π units, and each unit consists of c_0, l_0, and r_0. Meanwhile, n equals the cable length, of which the unit is kilometer.

As shown in Fig. 2, with the SWPE injected, the SWPR data (u_{1n}, i_{1n}, u_{2n}, and i_{2n}) are measured in the case of $n=24$ ($l=24$ km).

A. Optimization Effectiveness Validation of KF Algorithm for SWPR with Error

The parameter shift of cable aging can be a primary model error. The observation error is primarily caused by harmonics, instrumentation error, or Gaussian noise. Considering the effect of harmonics, instrumentation measuring shift, and Gaussian noise, the observation error can be represented by Gaussian noise with a mean value of 0.1 and a covariance value of 0.005. Two cases are disclosed as follows.

1) Case 1: Cable Line Parameter Fixed and SWPR Data with Error

In Fig. 9(a), u_1, u_{1n}, and u_{1op} represent the SWPR without error, SWPR injected into the Gaussian noise, and the optimization result of u_{1n} using the KF algorithm, respectively. It can be observed that u_1 and u_{1op} can overlap well, which means the error in u_{1n} can be filtered out well. Figure 9(b) illustrates the UIR curves. UIR_1, UIR_{1n}, and UIR_{1op} represent the UIR estimated using u_1, u_{1n}, and u_{1op} data, respectively. It can be observed that UIR_1 and UIR_{1op} can coincide well. However, UIR_{1n} deteriorates seriously due to the error in SWPR during the convolution inversion process. G_1, G_{1n}, and G_{1op} represent the amplitude-frequency characteristics calculated using UIR_1, UIR_{1n}, and UIR_{1op} data, respectively. It can be observed that G_1 and G_{1op} can coincide intensely with a slight difference in the high-frequency domain. For G_{1n}, the resonance point deviation is serious, and a severe ripple appears on the curve.

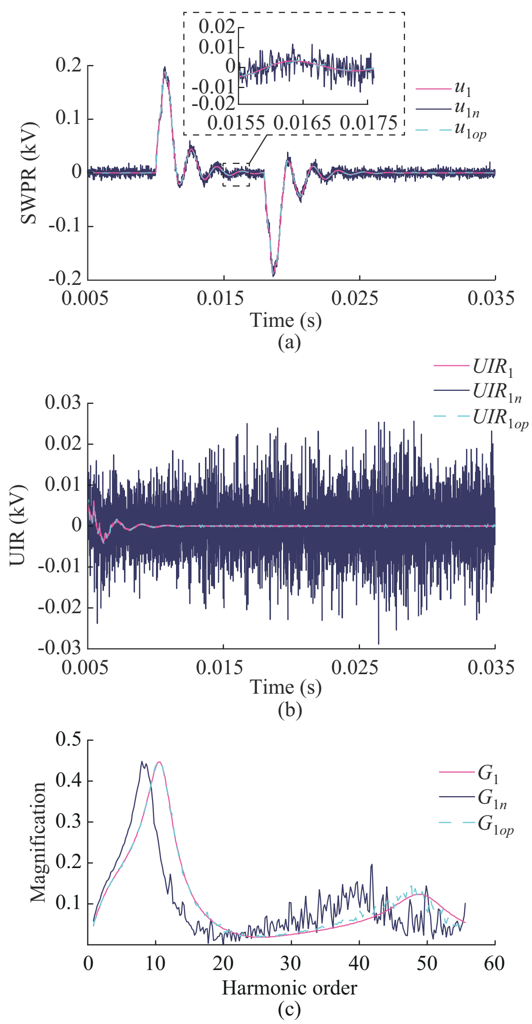

Fig. 9. Simulation curves of SWPR, UIR, and amplitude-frequency characteristics using KF algorithm. (a) SWPR. (b) UIR. (c) Amplitude-frequency characteristics using KF algorithm.

2) Case 2: Cable Line Parameter Shift and SWPR Data with Error

The actual parameters of cable line r_0, l_0, and c_0 shift to 0.85, 0.9, and 0.95 p.u., respectively. The measurement data (u_{1n} and u_{2n}) contain the error as case 1. Figure 10 shows the simulation curves of amplitude-frequency characteristics. $G_{u_1u_2n}$, $G_{u_1u_2}$, and $G_{u_1u_2op}$ represent the amplitude-frequency characteristics using u_{1n} and u_{2n} data, u_1 and u_2 data, and u_{1op} and u_{2op} data, respectively. It can be observed that $G_{u_1u_2op}$

and $G_{u_1u_2}$ overlap well. Likewise, $G_{u_1u_2n}$ and $G_{u_1u_2}$ have obvious deviation, which means that the model error and measurement error would lead to an inaccurate calculation for amplitude-frequency characteristics.

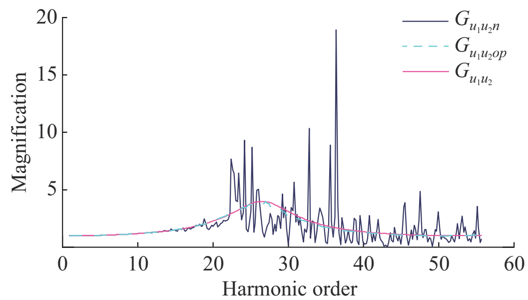

Fig. 10. Simulation curves of amplitude-frequency characteristics.

It can be concluded that the convolution inversion method is sensitive to measurement error, and the KF algorithm can optimize the SWPR data with error.

B. Accuracy Validation for HAF

In this subsection, the TF method as a standard is used to verify the accuracy of HAF obtained by the KFCI method, and the magnitudes of Z_0 and Z_g are chosen as the validation objects. According to (19), the HAF from current to a voltage obtained by the proposed method can be considered as a module of impedance obtained by the TF method.

The metric of root mean squared error (RMSE) is introduced to assess the performance of the KFCI method.

$$RMSE=\sqrt{\frac{1}{n}\sum_{i=1}^{n}(\alpha(i)-\beta(i))^2} \tag{23}$$

where $\alpha(i)$ and $\beta(i)$ represent the i^{th} element of vectors $\boldsymbol{\alpha}$ and $\boldsymbol{\beta}$, respectively. Figure 11 illustrates the HAF curves of Z_0 and Z_g obtained by the TF and KFCI methods. And schemes 2 and 3 are considered when calculating HAF using the KFCI method.

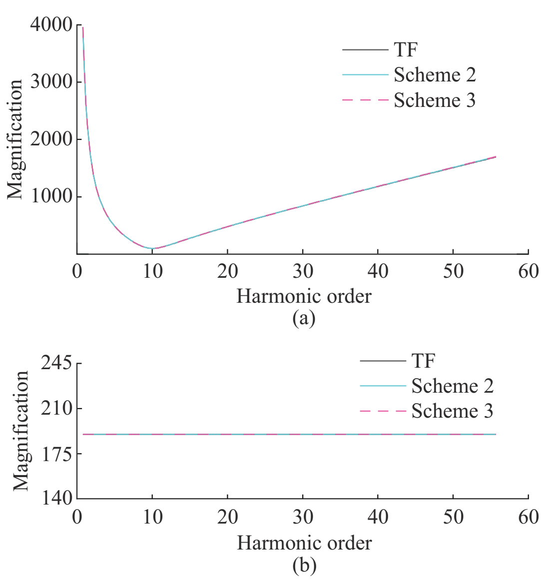

Fig. 11. HAF curves of Z_0 and Z_g obtained by TF and KFCI methods. (a) Z_0. (b) Z_g.

$RMSE_V$ represents the RMSE of the HAF obtained by scheme 2 and TF method, and $RMSE_D$ represents the RMSE of the HAF obtained by scheme 3 and TF method.

In Fig. 11(a), the HAF curves overlap well, and $RMSE_V$ and $RMSE_D$ are 1.0247×10^{-5} and 1.2106×10^{-5}, respectively. In Fig. 11(b), the HAF curves also overlap well, and $RMSE_V$ and $RMSE_D$ are 0.3247×10^{-5} and 0.1072×10^{-5}, respectively. Besides, the magnification is 190.4167 at the 3rd harmonic order, which coincides with the parameter of Z_g listed in Table II. It can be concluded that schemes 2 and 3 can obtain the module of impedance, which verifies the accuracy for HAF using the two injection schemes.

C. Rationality Validation of Harmonic Amplification Characteristic Analysis

This subsection only considers injecting harmonic voltage to validate the rationality of analysis of HAF for voltage presented in Section IV. And the cable length is set to be 24 km.

Case 1: G_{u_1} and G_{u_2} validation considering scheme 2. The current source is disconnected from the model built on PSCAD, as shown in Fig. 2. Then, the harmonic-voltage generator (u_0) emits the 12nd, 13rd, 14th, 15th, and 16th harmonics. As observed from Fig. 12, the total harmonic distortion (THD) of u_1 and u_2 is 4.65% and 6.67%, respectively. For the harmonic order range of 13rd to 16th, as shown in Fig. 4(a), G_{u_1} is about 0.19. Meanwhile, in Fig. 4(c), G_{u_2} is about 0.28. It can be found that the THD ratio (6.67%/4.65% = 1.4344) of the experimental result matches with the HAF ratio (0.28/0.19 = 1.4737) of the analytical result.

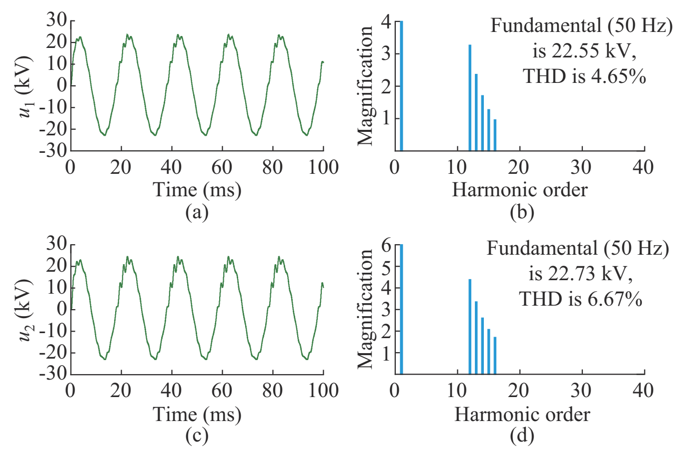

Fig. 12. Simulation waveforms and their frequency spectrums in case 1. (a) u_1. (b) Frequency spectrum of u_1. (c) u_2. (d) Frequency spectrum of u_2.

Case 2: H_{uu} validation considering scheme 3. The harmonic-voltage generator (u_0) and harmonic-current generator (i_0) emit the 23rd, 24th, 25th, 26th, and 27th harmonics synchronously. In Fig. 13, the THDs of u_1 and u_2 are 5.64% and 1.58%, respectively. For the harmonic order range of 23rd to 27th, as shown in Fig. 4(c), H_{uu} is about 0.265. Using the same comparison method as the case 1, the THD ratio (1.58%/5.64% = 0.28) matches with the value 0.265 of HAF.

It can be observed that harmonics could be amplified from the sending end to the grid end of the cable line. For instance, the THD of u_1 is 4.65%, and the THD of u_2 is

6.67% (already exceeding the THD standard of 5% [29]), as shown in Fig. 12.

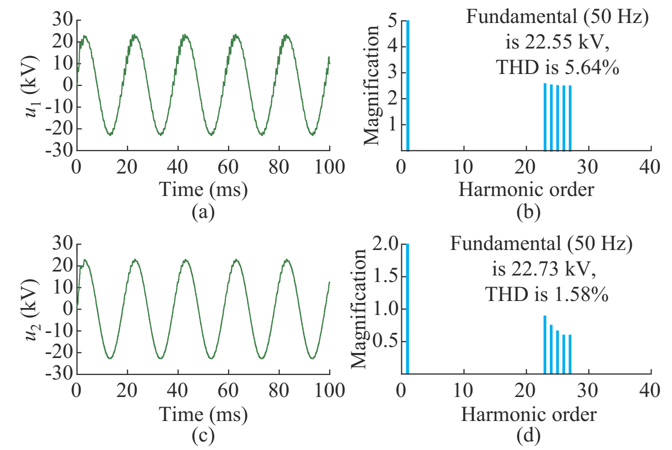

Fig. 13. Simulation waveforms and their frequency spectrums in case 2. (a) u_1. (b) Frequency spectrum of u_1. (c) u_2. (d) Frequency spectrum of u_2.

VI. Conclusion

The convolution inversion method combining the KF algorithm can obtain the HAF accurately using the SWPR data with error. The main harmonic amplification characteristics are drawn as follows.

1) The harmonic voltage generated by the sending generator would decrease when it arrives at both terminals of the cable line. The harmonic voltage from the sending end to the grid end of the cable line could not be amplified seriously. Harmonic current from the sending end to the grid end of the cable line would be amplified in a wide frequency band.

2) The distributed capacitance and inductance of the cable line significantly influence harmonic amplification.

Appendix A

$$\boldsymbol{J}=\begin{bmatrix} \rho(m) & \rho(m-1) & \cdots & \rho(1) & \rho(0) & 0 & \cdots & 0 \\ 0 & \rho(m) & \cdots & \rho(2) & \rho(1) & \rho(0) & \cdots & 0 \\ \vdots & \vdots & & \vdots & \vdots & \vdots & & \vdots \\ 0 & 0 & \cdots & \rho(m-1) & \cdots & \rho(m-2) & \cdots & \rho(0) \end{bmatrix} \tag{A1}$$

References

[1] J. F. C. Acero, W. R. L. Viamonte, N. J. B. C. Wilhem *et al*., "Harmonic distortion effects of the wind farm connected to the grid: case study for Marcona at 32 MW," in *Proceeding of 2021 IEEE PES/IAS Power Africa*, Nairobi, Kenya, Aug. 2021, pp. 1-5.

[2] K. Ji, H. Pang, J. Yang *et al*., "DC side harmonic resonance analysis of MMC-HVDC considering wind farm integration," *IEEE Transactions on Power Delivery*, vol. 36, no. 1, pp. 254-266, Mar. 2021.

[3] M. Badoni, A. Singh, S. Pandey *et al*., "Fractional-order notch filter for grid-connected solar PV system with power quality improvement," *IEEE Transactions on Industrial Electronics*, vol. 69, no. 1, pp. 429-439, Jan. 2022.

[4] G. Li, Y. Chen, A. Luo *et al*., "Wideband harmonic voltage feedforward control strategy of STATCOM for mitigating subsynchronous resonance in wind farm connected to weak grid and LCC HVDC," *IEEE Journal of Emerging and Selected Topics in Power Electronics*, vol. 9, no. 4, pp. 4546-4557, Sept. 2021.

[5] A. Argüello, "Setpoint feasibility and stability of wind park control interactions at weak grids," *Journal of Modern Power Systems and Clean Energy*, vol. 10, no. 6, pp. 1790-1796, Nov. 2022.

[6] Z. Xie, X. Gao, S. Yang *et al*., "Improved fractional-order damping method for voltage-controlled DFIG system under weak grid," *Journal of Modern Power Systems and Clean Energy*, vol. 10, no. 6, pp. 1531-1541, Nov. 2022.

[7] J. He, Y. Li, R. Wang *et al*., "Analysis and mitigation of resonance propagation in grid-connected and islanding microgrids," *IEEE Transactions on Energy Conversion*, vol. 30, no. 1, pp. 70-81, Jul. 2015.

[8] A. Terciyanli, M. Ermis, and I. Cadirci, "A selective harmonic amplification method for reduction of kVA rating of current source converters in shunt active power filters," *IEEE Transactions on Power Delivery*, vol. 26, no. 1, pp. 65-78, Nov. 2011.

[9] N. Parida and A. Das, "A modular multilevel converter with filter capacitor for long-cable-fed drive application," *IEEE Transactions on Industry Applications*, vol. 55, no. 6, pp. 7833-7842, Jul. 2019.

[10] X. Wang and F. Blaabjerg, "Harmonic stability in power electronic-based power systems: concept, modeling, and analysis," *IEEE Transactions on Smart Grid*, vol. 10, no. 3, pp. 2858-2870, Mar. 2019.

[11] Z. Chen, X. Huang, A. Luo *et al*., "Wideband harmonic resonance characteristics and coordinated damping method for distributed generation power plants," *IEEE Transactions on Industrial Electronics*, vol. 66, no. 10, pp. 7753-7764, Dec. 2019.

[12] Z. Liu, J. Rong, G. Zhao *et al*., "Harmonic assessment for wind parks based on sensitivity analysis," *IEEE Transactions on Sustainable Energy*, vol. 8, no. 4, pp. 1373-1382, Mar. 2017.

[13] Z. Huang, Y. Cui, and W. Xu, "Application of modal sensitivity for power system harmonic resonance analysis," *IEEE Transactions on Power Systems*, vol. 22, no. 1, pp. 222-231, Jul. 2007.

[14] Z. Zhang, W. Wu, Z. Shuai *et al*., "Principle and robust impedance-based design of grid-tied inverter with LLCL-filter under wide variation of grid-reactance," *IEEE Transactions on Power Electronics*, vol. 34, no. 5, pp. 4362-4374, Aug. 2019.

[15] L. An, X. Ning, Z. Shuai *et al*., "Large-scale photovoltaic plant harmonic transmission model and analysis on resonance characteristics," *IET Power Electronics*, vol. 8, no. 4, pp. 565-573, Apr. 2015.

[16] Y. Song, E. Ebrahimzadeh, and F. Blaabjerg, "Analysis of high-frequency resonance in DFIG-based offshore wind farm via long transmission cable," *IEEE Transactions on Energy Conversion*, vol. 33, no. 3, pp. 1036-1046, Jan. 2018.

[17] S. Habib and B. Kordi, "Calculation of multiconductor underground cables high-frequency per-unit-length parameters using electromagnetic modal analysis," *IEEE Transactions on Power Delivery*, vol. 28, no. 1, pp. 276-284, Nov. 2013.

[18] J. Angelov, J. Vuletic, R. Ackovski *et al*., "An extension in cable modeling for grounding system analysis," *IEEE Transactions on Industry Applications*, vol. 51, no. 6, pp. 5086-5094, Mar. 2015.

[19] Y. Song and C. Breitholtz, "Nyquist stability analysis of an AC-grid connected VSC-HVDC system using a distributed parameter DC cable model," *IEEE Transactions on Power Delivery*, vol. 31, no. 2, pp. 898-907, Dec. 2016.

[20] S. Zhang, S. Jiang, X. Lu *et al*., "Resonance issues and damping techniques for grid-connected inverters with long transmission cable," *IEEE Transactions on Power Electronics*, vol. 29, no. 1, pp. 110-120, Mar. 2014.

[21] A. Gargoom, A. M. Oo, and M. Cavanagh, "A method for calculating the asymmetry in the shunt parameters of power lines in compensated distribution networks," *IEEE Transactions on Power Delivery*, vol. 35, no. 5, pp. 2168-2176, Dec. 2020.

[22] C. Chen, H. Yang, W. Wang *et al*., "Harmonic transmission characteristics for ultra-long distance AC transmission lines based on frequency-length factor," *Electric Power Systems Research*, vol. 182, p. 106189, May 2020.

[23] Y. Pu, Q. Shu, J. Chang *et al*., "A method for estimating the amplitude-frequency characteristics of the cable line model with distributed parameters," *IEEE Transactions on Instrumentation and Measurement*, vol. 71, pp. 1-11, Sept. 2022.

[24] Y. Qi, H. Deng, J. Wang *et al*., "Passivity-based synchronization stability analysis for power-electronic-interfaced distributed generations," *IEEE Transactions on Sustainable Energy*, vol. 12, no. 2, pp. 1141-1150, Nov.2021.

[25] S. Liu, X. Li, M. Xia *et al*., "Takagi-sugeno multimodeling-based large signal stability analysis of DC microgrid clusters," *IEEE Transactions on Power Electronics*, vol. 36, no. 11, pp. 12670-12684, Apr. 2021.

[26] M. Todorovski and R. Ackovski, "Equivalent circuit of single-core cable lines suitable for grounding systems analysis under line-to-ground faults," *IEEE Transactions on Power Delivery*, vol. 29, no. 2, pp. 751-

759, Aug. 2014.
[27] L. Jing, W. Wang, Z. Li *et al*., "Detecting impedance and shunt conductance faults in lossy transmission lines," *IEEE Transactions on Antennas and Propagation*, vol. 66, no. 7, pp. 3678-3689, Apr. 2018.
[28] X. Yang, M.-S. Choi, S.-J. Lee *et al*., "Fault location for underground power cable using distributed parameter approach," *IEEE Transactions on Power Systems*, vol. 23, no. 4, pp. 1809-1816, Oct. 2008.
[29] *Power Quality: Harmonics in Public Power Grid*, GB/T 14549-93, 1994.

Yang Pu is currently pursuing the Ph. D. degree with Sichuan University, Chengdu, China. His main research interests include the stability and security of new energy generations.

Qin Shu received the B.S. degree in engineering with a major in power system and automation from Chongqing University, Chongqing, China, in 1982, the M.S. degree in engineering with a major in power system and automation from the University of Science and Technology, Chengdu, China, in 1986, and the Ph. D. degree with a major in signal and information processing from the University of Electronic Science and Technology of China, Chengdu, China, in 1991. He is currently a Professor with the College of Electrical Engineering, Sichuan University, Chengdu, China. His main research interests include modern signal processing, power system, and condition monitoring of power apparatus.

Fangwei Xu received the M.S. degree in electrical engineering from Chongqing University, Chongqing, China, in 2004, and the Ph. D. degree in power system and its automation from Sichuan University, Chengdu, China, in 2012. She is currently an Associate Professor with the College of Electrical Engineering, Sichuan University. Her main research interests include power quality and stability.